Crystal structures of Boro-AFm and sBoro-AFt phases

Jean-Baptiste Champenois [a], Adel Mesbah [a,b], Céline Cau Dit Coumes [a,*], Guillaume Renaudin [b,d], Fabrice Leroux [c,d], Cyrille Mercier [e], Bertrand Revel [f], Denis Damidot [g]

[a] Commissariat à l'Energie Atomique et aux Energies Alternatives, CEA DEN/DTCD/SPDE, F-30207 Bagnols sur Cèze, France
[b] Clermont Université, ENSCCF, Institut de Chimie de Clermont-Ferrand, BP 10448, F-63000 Clermont-Ferrand, France
[c] Clermont Université, Université Blaise Pascal, Institut de Chimie de Clermont-Ferrand, BP 10448, F-63000 Clermont-Ferrand, France
[d] CNRS, UMR 6296, ICCF, F-63171 Aubière, France
[e] LMCPA, Université de Valenciennes et du Hainaut Cambrésis, 59600 Maubeuge, France
[f] Centre Commun de Mesure RMN, Université Lille1 Sciences et Technologies, Cité Scientifique 59655 Villeneuve d'Ascq Cedex, France
[g] EM Douai, MPE-GCE, 59508 Douai, France

ARTICLE INFO

ABSTRACT

Crystal structures of boron-containing AFm (B-AFm) and AFt (B-AFt) phases have been solved *ab-initio* and refined from X-ray powder diffraction. ^{11}B NMR and Raman spectroscopies confirm the boron local environment in both compounds: three-fold coordinated in B-AFm corresponding to HBO_3^{2-} species, and four-fold coordinated in B-AFt corresponding to B $(OH)_4^-$ species. B-AFm crystallizes in the rhombohedral $R\bar{3}c$ space group and has the $3CaO \cdot Al_2O_3 \cdot CaHBO_3 \cdot 12H_2O$ ($4CaO \cdot Al_2O_3 \cdot 1/2B_2O_3 \cdot 12.5H_2O$, $C_4AB_{1/2}H_{12.5}$) general formulae with planar trigonal HBO_3^{2-} anions weakly bonded at the centre of the interlayer region. One HBO_3^{2-} anion is statistically distributed with two weakly bonded water molecules on the same crystallographic site. B-AFt crystallizes in the trigonal $P3c1$ space group and has the $3CaO \cdot Al_2O_3 \cdot Ca(OH)_2 \cdot 2Ca(B (OH)_4)_2 \cdot 24H_2O$ ($6CaO \cdot Al_2O_3 \cdot 2B_2O_3 \cdot 33H_2O$, $C_6AB_2H_{33}$) general formulae with tetrahedral B $(OH)_4^-$ anions located in the channel region of the structure. All tetrahedral anions are oriented in a unique direction, leading to a hexagonal c lattice parameter about half that of ettringite.

1. Introduction

Borate anions are frequently encountered in low- and intermediate-level (LLW and ILW) radioactive waste streams since boric acid is used as a neutron moderator in the water cooling system of pressurised water reactors (PWRs). The most widely used process for stabilization/solidification of such wastes is cementation. Borates are however reported to be strong retarders of Portland cement setting and hardening [1–4]. Retardation may arise from surface adsorption, and possibly from the formation of protective layers over cement grains due to precipitation with calcium [5]. According to Roux [6], and in agreement with the observations of Casabonne Masonnave [7], the borate inhibition effect might result from the formation of amorphous $2CaO \cdot 3B_2O_3 \cdot 8H_2O$ from polyboric anions $B_3O_3 (OH)_4^-$ and/or $B_3O_3 (OH)_5^{2-}$ when pH is within the range 4.5–12. At higher pH, aqueous boron, mainly as B $(OH)_4^-$, would precipitate into crystallized $CaO \cdot B_2O_3 \cdot 6H_2O$ or $CaO \cdot B_2O_3 \cdot 4H_2O$, which would allow cement hydration to progress. Three main strategies have thus been used to cement wastes with high contents of borates:

– use of a Portland cement blended with calcium hydroxide to precipitate borates as calcium hexahydroborite $CaO \cdot B_2O_3 \cdot 6H_2O$, which is later destabilized in favour of a boron-AFt phase (named B-AFt in the present text) in the hydrated cement paste [8,9],
– use of Portland cement blended with calcium aluminate cement (Fondu® type) and calcium hydroxide to incorporate borates directly into the following AFt phase: $3CaO \cdot Al_2O_3 \cdot 2Ca (B (OH)_4)_2 \cdot Ca (OH)_2 \cdot 30H_2O$ (calcium quadriboroaluminate QBA, or high boron-content AFt) [6,10,11],
– use of a calcium sulfoaluminate cement [12–14], possibly blended with Portland cement [15], to precipitate borates into a mixed borate/sulphate AFt phase.

The B-AFt phases thus play a key role in the insolubilization of borate ions. AFt (calcium *a*luminate or *f*errite *t*ri-substituted hydrates) stands for a large group of minerals which refers to ettringite $3CaO \cdot Al_2O_3 \cdot 3CaSO_4 \cdot 32H_2O$. Their general formulae can be written $3CaO \cdot (Al,Fe)_2O_3 \cdot 3CaX_2 \cdot nH_2O$ where X is one monovalent anion or half a divalent anion. The crystal structure is composed of positively charged columns $[Ca_3Al (OH)_6 \cdot 12H_2O]^{3+}$ arranged parallel to the c lattice parameter from a hexagonal unit cell, and of negatively charged channels $[3X \cdot nH_2O]^{3-}$. Trivalent Al^{3+} can be substituted by Fe^{3+}, Cr^{3+}, Mn^{4+} or Si^{4+} [16–18]. AFt phases are known to bind

* Corresponding author.
  E-mail address: celine.cau-dit-coumes@cea.fr (C. Cau Dit Coumes).

many anions such as SO_4^{2-}, SO_3^{2-}, OH^- [19,20], SeO_4^{2-}, CrO_4^{2-} or VO_4^{3-} [21,22]. The incorporation of borate anions in the AFt phase is also well documented. Wenda and Kuzel [23] showed that borate can substitute completely for sulphate in the ettringite structure. They reported the existence of two boron-containing AFt phases, one ($C_3A\cdot Ca$ (B $(OH)_4)_2.Ca$ $(OH)_2\cdot 36H_2O$) with a high and the other ($C_3A\cdot Ca$ (B $(OH)_4)_2\cdot 2Ca$ $(OH)_2.36H_2O$) with a low boron content. IR spectroscopy showed boron to be four-coordinated within the AFt structure (*i.e.* existing as tetrahedral B $(OH)_4^-$ anion). Poellmann et al. [24] additionally demonstrated that a large range of solid solutions existed between ettringite and the high or low boron-content AFt phases. Compounds with intermediate boron-content from the solid solution $3CaO\cdot Al_2O_3\cdot xCa$ $(OH)_2\cdot (3-x)$ Ca (B $(OH)_4)_2\cdot nH_2O$ with $1\leq x\leq 2$, have also been reported [25]. Nevertheless, no detailed crystallographic data are available for the boron-containing AFt phase.

AFm phases, which can be formed in significant amounts by hydrating calcium aluminate cement [26] or a calcium sulfoaluminate cement with a low calcium sulphate content [27], are also interesting candidates to insolubilize borate ions. AFm phases (calcium *A*luminate or *F*errite *M*ono-substituted hydrates) belong to the layered double hydroxide (LDH) large family. Their general formulae can be written $3CaO\cdot (Al,Fe)_2O_3\cdot CaX_2\cdot nH_2O$ where X is one monovalent anion or half a bivalent anion. Their crystal structure is composed of positively charged main layer $[Ca_2(Al,Fe)$ $(OH)_6]^+$ and negatively charged interlayer $[X\cdot nH_2O]^-$. A variety of anions can be incorporated, such as SO_4^{2-} [28], Cl^- [29–31], CO_3^{2-} [32,33], NO_3^- [34,35], I^- and Br^- [36,37]. The incorporation of borate anion in the interlayer region leads to $4CaO\cdot Al_2O_3\cdot 1/2B_2O_3\cdot 12H_2O$, called calcium monoboroaluminate hydrate (named B-AFm here). No crystallographic data have been reported yet for B-AFm and the boron environment has still to be clarified [38–40]. Based on the existence of a complete solid solution between B-AFm and the hemicarboaluminate $4CaO\cdot Al_2O_3\cdot 1/2CO_2\cdot 12H_2O$, Bothe and Brown postulated a three-fold coordination of boron in B-AFm (*i.e.* HBO_3^{2-}) as for CO_3^{2-} [39,40]. According to Cszetenyi [25], the B-AFm compound exhibits a FT-IR spectrum similar to those of compounds based on a boron-oxygen ring with $[B_3O_3$ $(OH)_5]^{2-}$ composition. Boron atoms would thus rather form such rings in the B-AFm interlayer.

The objective of this work was thus to give an accurate description of the structures of both B-AFm and high B-AFt ($3CaO\cdot Al_2O_3\cdot Ca$ $(OH)_2\cdot 2Ca$ (B $(OH)_4)_2\cdot nH_2O$) phases using X-ray powder diffraction, ^{11}B NMR and Raman spectroscopy.

2. Experimental

2.1. Sample preparation

Powder samples with nominal composition $4CaO\cdot Al_2O_3\cdot 1/2B_2O_3\cdot nH_2O$ and $6CaO\cdot Al_2O_3\cdot 2B_2O_3\cdot nH_2O$ were synthesized in stirred aqueous suspension. Tricalcium aluminate ($3CaO\cdot Al_2O_3$), lime (VWR≥99%) which was heated at 950 °C for 12 h to obtain pure calcium oxide CaO, and boric acid (H_3BO_3, VWR≥99%) were mixed in pure boiled and decarbonated water with molar ratios equal to 1:1:1 and 1:3:4, respectively. Boric acid was introduced in slight excess (weight overestimated by 1%) to ensure a complete reaction of tricalcium aluminate ($3CaO\cdot Al_2O_3$). All experiments were carried out in a CO_2-free atmosphere.

Boric acid was first dissolved in water. Calcium oxide was then introduced in order to form calcium hexahydroborite $CaO\cdot B_2O_3\cdot 6H_2O$. This step enabled to avoid the dissolution inhibition of tricalcium aluminate by borate anions. Tricalcium aluminate was then added, and the mixture was stored under stirring conditions during 7 days and 90 days respectively at room temperature (20 ± 1 °C). Mixtures were then filtered at 0.45 μm. Solid fractions were dried with isopropanol and stored away from CO_2.

2.2. X-ray powder diffraction

X-ray powder diffraction (XRPD) data of B-AFm were collected on a D8 Advance (Bruker) diffractometer equipped with a Göbel mirror and a Lynx Eye detector. The B-AFm sample was measured using the Debye Scherrer geometry (transmission mode). The sample was introduced in a Lindeman tube ($\Phi = 1$ mm) and mounted on a spinning goniometric head during measurement to reduce the preferred orientation effect. Data were recorded by using copper radiation ($\lambda = 1.5418$ Å) at room temperature in the 2θ range 4–120° with a step size of 0.011° for a total counting time of 8 h.

The XRPD pattern of B-AFt was recorded with the Bragg Brentano geometry on the Bruker D8 Advance diffractometer (2θ angular range between 5 and 120°, step size of 0.019° for a total counting time of 4 h). Pure silicon was measured under the same conditions to extract the instrumental resolution function.

For both compounds, diffraction maxima were located using standard peak search methods with reflex from MSModeling program [41]. X-Cell [42] was used for indexing the powder patterns. Localization of the atoms in the unit cell was determined with the EXPO program [43] working on the previously extracted intensities. Rietveld refinement of the structure was then performed using the Full-Prof_Suite program [44]. The structures were refined down to $R_p = 0.037$, $R_{wp} = 0.059$, $R_{Bragg} = 0.11$ and $R_F = 0.10$ Rietveld factors for B-AFm, and $R_p = 0.049$, $R_{wp} = 0.068$, $R_{Bragg} = 0.064$ and $R_F = 0.08$ for B-AFt.

2.3. Differential scanning calorimetry and thermogravimetric analyses (DSC and TGA)

Differential scanning calorimetry (DSC) and thermogravimetric analyses (TGA) were performed with a Netzsch STA 409 PC instrument between 20 °C and 1000 °C under nitrogen atmosphere with a heating rate of 2 °C/min. The curves were corrected from buoyancy effects (caused by the density of the surrounding gas decreasing on heating) by performing a blank subtraction.

2.4. Micro Raman spectroscopy

Micro-Raman spectra were recorded at room temperature in the back scattering geometry, using a Jobin-Yvon T64000 device. The spectral resolution obtained with an excitation source at 514.5 nm (argon ion laser line, Spectra Physics 2017) was about 1 cm^{-1}. The Raman detector was a charge coupled device (CCD) multichannel detector cooled by liquid nitrogen to 140 K. The laser beam was focused onto the sample through an Olympus confocal microscope with ×100 magnification. Laser spot was about 1 μm^2. Measured power at the sample level was kept low (less than 10 mW) in order to avoid any damage of the material. The Raman scattered light was collected with the microscope objective at 180° from the excitation and filtered with an holographic Notch filter before being dispersed by a single grating (1800 grooves per nm). Spectra were recorded (four scans of 300 s each) in the frequency range 300 cm^{-1}–1600 cm^{-1} in order to investigate the Raman active vibration modes of borate groups.

2.5. ^{11}B NMR spectroscopy

The B-AFm and B-AFt phases were characterized using ^{11}B and ^{1}H MAS NMR. The [11]B MAS spectra were recorded at a Larmor frequency of 256.7 MHz using a Bruker Advance III 800 MHz (18.8 T) spectrometer. The spectra were made up of 64 free induction decays with a pulse length of 1 μs (π/10) and a relaxation delay of 5 s. The samples were spun at 20 kHz in 3.2 mm probe. Experimental referencing, calibration, and setup were performed using solid powdered sodium borohydride. Solid $NaBH_4$ has a chemical shift of -42.06 ppm relative to the primary
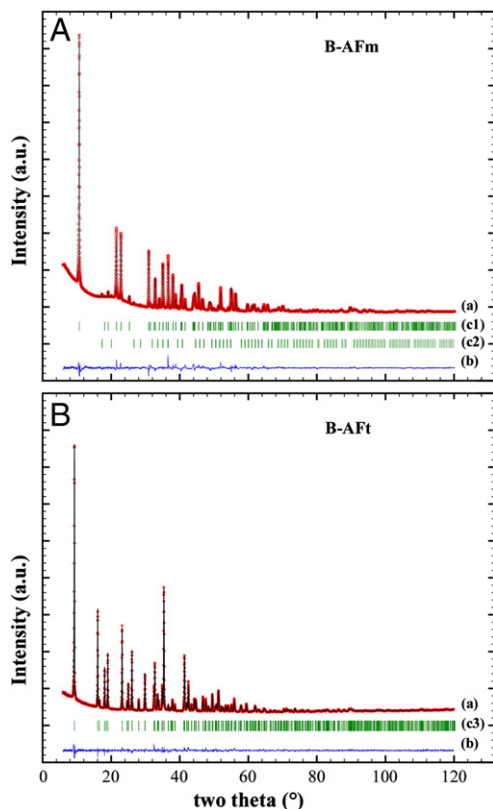
Fig. 1. Rietveld plots for the B-AFm (top) and the B-AFt (bottom) samples: experimental and calculated powder patterns (a), difference curves (b) and Bragg peak positions for the B-AFm phase (c1), katoite (c2) and the B-AFt phase (c3).

standard, liquid $F_3B\cdot O$ (C_2H_5)$_2$ (where $\delta(^{11}B) = 0.00$ ppm). The baseline was corrected by subtracting the background signal coming from the boron nitride stator of the probe. In complementary experiments, the boron NMR spectra were proton decoupled by applying a proton decoupling field of 80 kHz. Spectral decomposition was performed using DMFit software [45].

2.6. Scanning electron microscopy

The morphologies of B-AFm and B-AFt crystals were observed using scanning electron microscopy (FEI Inspect S50, equipped with a tungsten filament, acceleration voltage = 15 kV, filament current = 50 μA). The powders were previously dispersed in ethanol

using an ultrasonic bath. A drop of suspension was then laid down on a carbon film. Ethanol was evaporated, and the powders were carbon-coated under vacuum before observation.

2.7. ICP-AES analysis

The chemical compositions of the synthesized phases were determined by ICP-AES analyses. The powders were dissolved in a small volume of concentrated nitric acid (1 mol/L), and the resulting solutions were analysed for Ca, Al, and B using ICP-AES (Vista Pro Varian, standardization with matrix reconstitution).

3. Results

3.1. Chemical compositions

The B-AFm sample was almost single phase after seven days of reaction. Its X-ray powder pattern could be indexed using a hexagonal unit cell with the following refined lattice parameters: $a = 5.7764$ (1) Å and $c = 49.5499$ (9) Å. Small amounts of katoite (about 3 wt.% according to subsequent Rietveld refinement) were present as impurity. This was in agreement with the phase equilibrium diagram of the $CaO–Al_2O_3–B_2O_3–H_2O$ system established by Bothe and Brown [40], showing the coexistence of B-AFm and katoite.

The B-AFt sample was single phase after 90 days under stirring conditions. The whole powder pattern was indexed using a hexagonal unit cell with the following refined lattice parameters: $a = 11.0295$ (1) Å and $c = 10.6990$ (1) Å. Rietveld plots are shown in Fig. 1.

Raman spectroscopy revealed a slight carbonate contamination of the B-AFm sample (Fig. 2). The spectrum exhibited a vibration at 1089 cm^{-1} which is characteristic of weakly bonded carbonate anions in the interlayer region of AFm phases [46]. Carbonate contamination of the B-AFt sample was not obvious since the signal at 1075 cm^{-1} could be assigned to a borate anion vibration.

Chemical compositions of B-AFm and B-AFt phases were determined using ICP-AES and TGA analyses. Their atomic ratios Ca:Al:B were found to be 4.00:2.07:1.05 and 6.00:2.28:4.00 for B-AFm and B-AFt respectively. In both cases, the Ca:B and Al:B ratios were close to the expected composition: Ca:B = 3.8 ± 0.2 and Al:B = 1.97 ± 0.05 (confidence intervals taking into account errors due to ICP-AES analysis only) for B-AFm with the nominal $4CaO\cdot Al_2O_3\cdot 1/2B_2O_3\cdot nH_2O$ composition, and Ca:B = 1.50 ± 0.04 and Al/B = 0.57 ± 0.02 for B-AFt with the nominal $6CaO\cdot Al_2O_3\cdot 2B_2O_3\cdot nH_2O$ composition. The small surplus of aluminium in the AFt phase analysis might have indicated a slight contamination by amorphous aluminium hydroxide. However, the thermogram of the final product did not exhibit any weight loss characteristic of aluminium hydroxide dehydration (main loss at
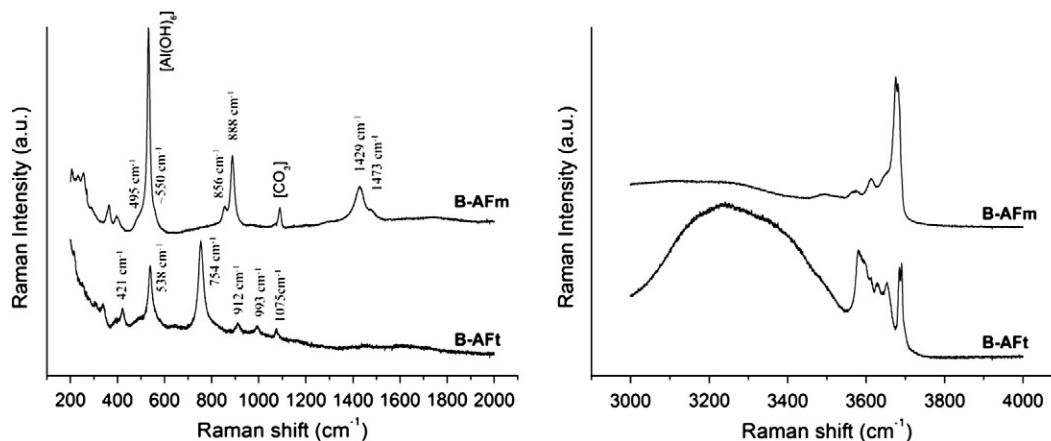

Fig. 2. Micro-Raman spectra of B-AFm and B-AFt samples. Spectral ranges corresponding to the vibrations of the borate groups (left) and of the hydrogen bond networks (right).
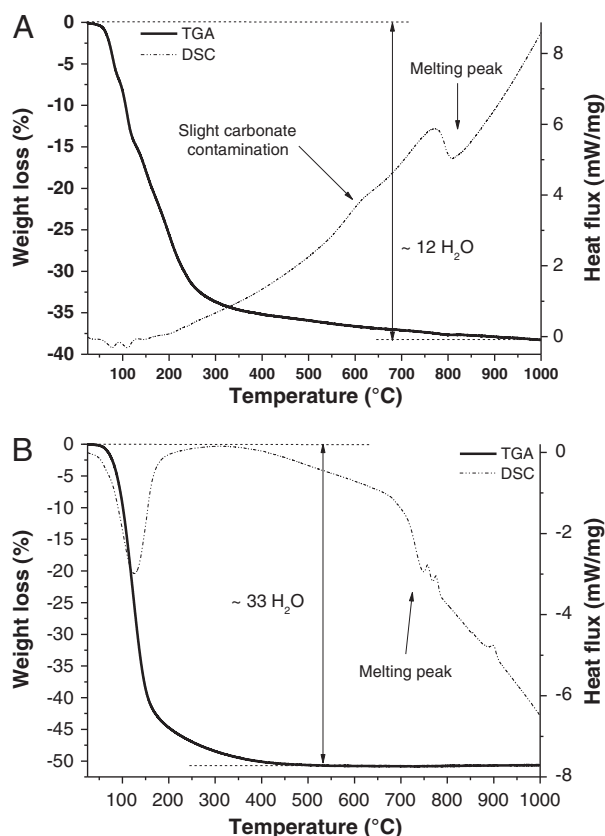
Fig. 3. TGA/DSC analysis of B-AFm (A) and of B-AFt (B).

Table 2
Atomic coordinates, isotropic thermal displacement and occupancy parameters for the B-AFm hydrate.

Atom	Wyckoff					
Site	x	y	z	B_{iso} (Å²)	Occupancy	
Al	6b	0	0	0	0.66 (3)	1
Ca	12c	1/3	2/3	0.01127 (2)	=U$_{eq}$(Al)	1
Oh	36f	0.7507 (3)	0.6889 (4)	0.02055 (3)	=U$_{eq}$(Al)	1
Ow1	12c	1/3	2/3	0.06235 (7)	3.8 (2)	1
B	6a	0	0	1/4	=U$_{eq}$(Ow1)	0.5 (−)
Ob	18e	0	0.2170 (5)	1/4	=U$_{eq}$(Ow1)	0.5 (−)
Ow2	18e	=(Ob)	=y(Ob)	=z(Ob)	=U$_{eq}$(Ow1)	0.38 (1)

From these results, the chemical compositions of B-AFm and B-AFt were assessed to be $4CaO \cdot Al_2O_3 \cdot 1/2B_2O_3 \cdot 12H_2O$ and $6CaO \cdot Al_2O_3 \cdot 2B_2O_3 \cdot 33H_2O$ respectively.

3.2. Crystal structure of the B-AFm phase

Indexation of the X-ray powder pattern showed that the B-AFm structure is described in the trigonal system: $R\bar{3}c$ space group with refined lattice parameters $a = 5.7764$ (1) Å and $c = 49.5499$ (9) Å for a unit cell volume $V = 1431.83$ (4) Å³ (see Table 1). Le-Bail fitting led to good R factors with $R_p = 0.028$ and $R_{wp} = 0.04$. A c hexagonal axis close to 50 Å is a characteristic of a 6R polytype with the $R\bar{3}c$ symmetry [48]. B-AFm phase crystallizes in the same space group than Friedel's salt (the HT-polymorph or the slightly carbonated Friedel's salt) [30,31,50], the mixed chloro-carboaluminate AFm phase [46,49], and the iron containing AFm monocarbonate [50]. Crystal structure was solved by direct methods with EXPO and refined by Rietveld refinement with FullProf, leading to the conventional Rietveld factors $R_p = 0.041$ and $R_{wp} = 0.059$. Borate anions were described by planar trigonal [BO$_3$] entities (hydrogen atoms belonging to the borate anions were not considered here due to the weak X-ray scattering contrast of H, as well as hydrogen atoms from hydroxyls and water molecules). The Rietveld plot is shown in Fig. 1 and the refinement parameters are given in Table 1.

The refined atomic parameters of the 7 non hydrogen atoms are summarized in Table 2 and a general representation of the B-AFm structure is shown in Fig. 4. The structure of B-AFm was composed of positively charged main layers [Ca$_2$Al (OH)$_6$]$^+$ and negatively charged interlayers [1/2HBO$_3 \cdot 3.14(1)$H$_2$O]$^-$. In order to ensure electroneutrality of the compound, refined trigonal [BO$_3$] entities should present two negative charges corresponding to the triangular

255 °C). The assumption of an Al surplus in the structure of the B-AFt phase was contradicted by Rietveld refinement of this phase (see Section 3.3). The slight aluminium excess was more likely due to experimental error.

The weight losses recorded between 25 °C and 1000 °C by TGA corresponded to the departure of 12 water molecules for the B-AFm phase and 33 water molecules for the B-AFt phase (Fig. 3). It should be noted however that, in this latter case, the amount of water molecules per formula unit may be slightly underestimated as AFt phases are very sensitive to dehydration [47].

Table 1
Refinement parameters for B-AFm and B-AFt.

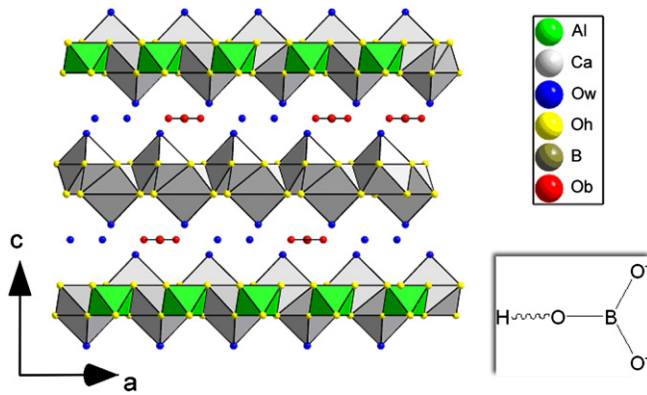| Compound	B-AFm	B-AFt
Formula	$3CaO \cdot Al_2O_3 \cdot CaHBO_3 \cdot 12.28(6)H_2O$	$3CaO \cdot Al_2O_3 \cdot Ca (OH)_2 \cdot 2Ca (B (OH)_4)_2 \cdot 24H_2O$
Structural formula	[Ca$_2$Al (OH)$_6$]$^+$[1/2HBO$_3 \cdot 3.14(3)$H$_2$O]$^-$	[Ca$_3$Al (OH)$_6 \cdot 9H_2O$]$^{3+}$[2B (OH)$_4 \cdot$OH$\cdot 2H_2O$]$^{3-}$
Formula weight (g.mol^{-1})	551.98	1172.34
T (K)	293 K	293 K
System	Trigonal	Trigonal
Space group	$R\bar{3}c$	$P\bar{3}c1$
a (Å)	5.7764 (1)	11.0296 (1)
c (Å)	49.5499 (9)	10.6992 (1)
V (Å³)	1431.82 (4)	1127.16 (2)
Z/Dx (g cm^{-3})	3/1.92	1/1.72
Wavelength (Å)	1.54184	1.54184
Angular range 2θ (°)	4.06–120.21	5.11–119.98
N$_{obs}$	10,560	6047
N$_{ref}$	534	1210
R$_p$	0.041	0.049
R$_{wp}$	0.058	0.068
R$_{Bragg}$	0.083	0.064
R$_F$	0.10	0.080
N of profile parameters	12	14
N intensity dependent parameters	10	18

Fig. 4. General representation of the B-AFm structure along [010]. For clarity reasons, the statistical distribution between one borate group and two water molecules was ordered in the figure. Geometry of the trigonal borate HBO_3^{2-} anion is shown in inset.

HBO_3^{2-} anion. The main layers contained ordered Al^{3+} cations in octahedral hydroxyl coordination, and seven-fold coordinated Ca^{2+} cations (6 hydroxyl anions + 1 water molecule from interlayer labelled Ow1), as usually encountered for AFm phases. The structure of B-AFm was described by 7 non-H atomic positions attributed to aluminium, calcium, hydroxyl ions (labelled Oh), water molecule bonded to Ca^{2+} (labelled Ow1), water molecule weakly bonded in the centre of the interlayer (labelled Ow2 with a refined partial occupancy of 0.38 (1)), boron atom from borate group (with a fixed partial occupancy of 1/2 in agreement with the determined chemical composition and for electroneutrality reason) and oxygen atoms from borate group (labelled Ob). The interlayer region was characterized by a statistic distribution between one trigonal borate anion and about two water molecules (Ob site and Ow2 site indicated in Table 2 correspond to a unique crystallographic site with a global occupancy of 0.88 (1)). Raman spectrum in the spectral range 3000 cm^{-1} to 4000 cm^{-1} with definite but broad signals agreed with such a static disorder involving the hydrogen bond network (Fig. 2). The refined composition $3CaO \cdot Al_2O_3 \cdot CaHBO_3 \cdot 12.3$ (1) H_2O was in agreement with the previously determined chemical composition $3CaO \cdot Al_2O_3 \cdot CaHBO_3 \cdot 12.H_2O$, namely in terms of water content. Interatomic distances, given in Table 3, are good indicators of the accuracy of the refined structural model. The unrealistic Ow2–Ow2 distance of 2.17 Å was explained by the statistic disorder in the interlayer region which banned the refinement of exact positional parameters for the Ow2 site (Ow2 site was combined with the Ob2 site to avoid strongly correlated parameters and to stabilize the Rietveld refinement).

Table 3
Selected interatomic distances in the B-AFm and B-AFt structures.

B-AFm			B-AFt		
Al	6×OH	1.937 (2)	Al	3×Oh1	1.822 (17)
				3×Oh2	2.06 (2)
Ca	3×Oh	2.394 (2)	Ca	Oh1	2.361 (17)
	3×Oh	2.438 (2)		Ow1	2.418 (17)
	Ow1	2.531 (4)		Oh2	2.437 (18)
				Oh2	2.47 (2)
				Ow2	2.503 (19)
				Oh1	2.513 (17)
				Ow3	2.599 (6)
				O	3.540 (12)
B	3×Ob	1.253 (3)	B1	Ob11	1.45 (3)
				3×Ob12	1.461 (13)
			B2	Ob21	1.39 (3)
				3×Ob22	1.46 (2)
Ob/Ow2	Ow1	2.556 (2)	O	Ob11	2.473 (13)
Ow2	Ow2	2.171 (4)		Ow3	2.715 (12)
				Ob12	2.99 (3)
				Ob12	3.10 (3)
				Ow1	3.12 (2)

Raman spectra of B-AFm and assignments (Fig. 2) agreed with the trigonal symmetry of borate HBO_3^{2-} anion [51]. Splitting of normal modes of vibration resulted from the fact that the real point symmetry of the HBO_3^{2-} anion located in the centre of the interlayer region was C_2, and not the apparent D_{3h} point symmetry of the 6a Wyckoff site from the $R\bar{3}c$ space group. Because of the presence of one hydrogen atom located in one among the three oxygen atoms, the trigonal symmetry of the free borate anion was lost in favour of the C_{2v} symmetry. According to previous works, planar HBO_3^{2-} anion is evidenced by the signals at 495 cm^{-1} and ~550 cm^{-1} (ν_s(B−O) superimposed with signal from octahedral [Al (OH)$_6$] group [46]), 856 cm^{-1} and 888 cm^{-1} (ν_s(B−O)) and 1429 cm^{-1} and 1473 cm^{-1} (ν_{as}(B−O)). The Raman signal at 1088 cm^{-1} was a characteristic of carbonate contamination of the AFm phase, with carbonate weakly bonded at the centre of the interlayer region (i.e. same location than HBO_3^{2-} borate anions) [46]. The weak signal observed at 1171 cm^{-1} for boric acid with trigonal B (OH)$_3$ entities, assigned to ν_{as}(B−O) [51], was not observed here. Assignment of the borate modes of vibration was complicated by the presence of natural boron containing the two ^{10}B (19.6%) and ^{11}B (80.4%) isotopes. ^{10}B to ^{11}B shifts were expected for asymmetric modes of vibration. For example, relative intensities of the signals at 1429 cm^{-1} and 1473 cm^{-1} could be correlated to the relative amounts of ^{11}B (signal at 1429 cm^{-1}) and ^{10}B (signal at 1473 cm^{-1}).

The local borate organisation in the B-AFm phase was also studied by ^{11}B NMR. The spectrum (Fig. 5) presented one main and broad peak for chemical shifts between 10 and 20 ppm, with a maximum at 15.9 ppm, which was a characteristic of tricoordinated B[III] atoms. ^{11}B (80.22% naturally abundant) is a half-integer nucleus (I = 3/2) that possesses a quadrupolar momentum. This gives rise to a quadrupolar interaction, the amplitude of which strongly depends on the distortion of the site compared to the cubic symmetry. When this interaction is strong, the second-order terms of the interactions are only partially averaged by MAS, and this results in a characteristic lineshape that can be seen in Fig. 5 for the B[III] sites. The splitting of the signal induces an experimental broadening and additionally shifts the peak to the lower ppm region [52–54]. On the contrary, for tetrahedral B[IV] sites, the higher symmetry corresponds to a small quadrupolar coupling constant, and the signals are nearly Gaussian [55,56]. The spectra recorded with and without any proton-decoupling field were very similar, showing that the B−H coupling was weak, which could result from a fast exchange of the hydrogen atoms on the NMR time scale. The presence of a very weak peak at 1.6 ppm was a characteristic of tetrahedral boron [52] and was assigned to a slight contamination.

3.3. Crystal structure of the B-AFt phase

Indexation of the X-ray powder pattern showed that the B-AFt structure is also described in the trigonal system: $P3c1$ space group
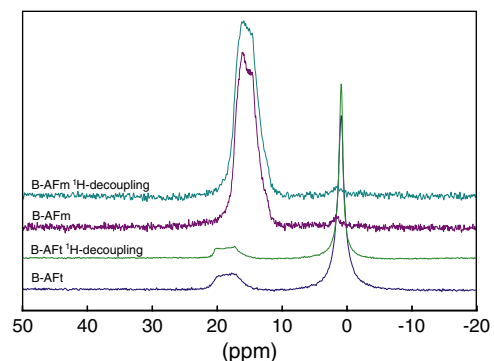

Fig. 5. ^{11}B MAS NMR with, and without, ^{1}H decoupling of B-AFm and B-AFt phases.

Table 4
Atomic coordinates, isotropic thermal displacement and occupancy parameters for the B-AFt hydrate.

Atom	Wyckoff site	x	y	z	B_{iso} (Å^2)	Occupancy
Ca	6d	0.3330 (4)	0.4725 (3)	0.4007 (15)	2.19 (5)	1
Al	2b	1/3	2/3	0.1397 (18)	1.9 (1)	1
Oh1	6d	0.4637 (11)	0.8077 (11)	0.0430 (17)	0.6 (1)	1
Oh2	6d	0.4783 (11)	0.6639 (17)	0.2591 (17)	$=U_{eq}$(Oh1)	1
Ow1	6d	0.3523 (12)	0.3096 (9)	0.2624 (15)	0.50 (9)	1
Ow2	6d	0.3131 (10)	0.3131 (8)	0.5759 (16)	$=U_{eq}$(Ow1)	1
Ow3	6d	0.0808 (7)	0.2580 (6)	0.4082 (18)	$=U_{eq}$(Ow1)	1
B1	2c	2/3	1/3	0.6319 (17)	4.2 (2)	1
B2	2a	0	0	0.6505 (18)	$=U_{eq}$(B1)	1
Ob11	2c	2/3	1/3	0.4964 (17)	$=U_{eq}$(B1)	1
Ob12	6d	0.6206 (14)	0.1872 (10)	0.661 (2)	$=U_{eq}$(B1)	1
Ob21	2a	0	0	0.5206 (16)	$=U_{eq}$(B1)	1
Ob22	6d	0.9094 (14)	0.0556 (16)	0.685 (2)	$=U_{eq}$(B1)	1
O	6d	0.6862 (10)	0.5538 (7)	0.419 (2)	4.3 (3)	1

with refined lattice parameters $a = 11.0296$ (1) Å, $c = 10.6992$ (1) Å for a unit cell volume $V = 1127.16$ (2) Å^3 (see Table 1). Le-Bail fitting led to good R factors with $R_p = 0.037$ and $R_{wp} = 0.05$. The space group, as well as the hexagonal c axis length, differed from those of ettringite ($P31c$ space group with $c \sim 21.45$ Å [57]). The hexagonal c lattice parameter was about half that of ettringite, whereas the basal parameter was equivalent (around 11 Å), indicating that the unit cell of B-AFt contained one $3CaO \cdot Al_2O_3 \cdot Ca(OH)_2 \cdot 2Ca$ (B$(OH)_4)_2 \cdot nH_2O$ motif ($Z = 1$). The crystal structure was solved by direct methods with EXPO, and refined by Rietveld refinement with FullProf, leading to the conventional Rietveld factors $R_p = 0.049$ and $R_{wp} = 0.068$ (Fig. 1, Table 1). Borate anions were described by tetrahedral [BO$_4$] entities corresponding to tetrahedral B$(OH)_4^-$ anions (hydrogen atoms belonging to the borate anions were not considered here due to the weak X-ray scattering contrast of H, like all other hydrogen atoms).
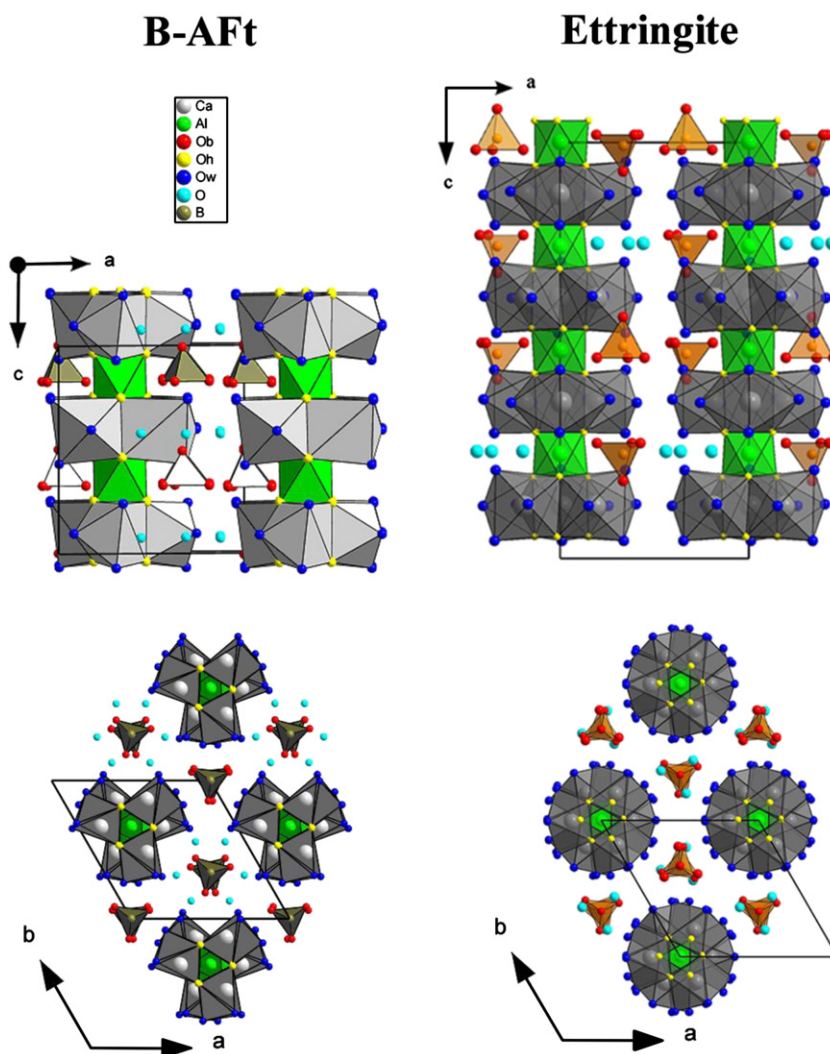

Fig. 6. Projection of the B-AFt structure (left) along the b axis (top) and along the c axis (bottom). Comparison with the ettringite structure is represented (right) by using equivalent colour codes.

The refined positions of the 14 non hydrogen atoms are reported in Table 4 and a general representation of the B-AFt structure is given in Fig. 6. Interatomic distances are given in Table 3. The structure of B-AFt was composed of positively charged columns $[Ca_3Al(OH)_6 \cdot 9H_2O]^{3+}$ arranged parallel to the c lattice parameter, and of negatively charged channels $[2B(OH)_4 \cdot OH \cdot 2H_2O]^{3-}$. The main columns contained trivalent Al^{3+} in hydroxyl octahedral coordination and bivalent Ca^{2+} cations, which were seven-fold coordinated with four hydroxyl groups (labelled Oh1 and Oh2) and three bonded water molecules (labelled Ow1, Ow2 and Ow3). The eighth neighbouring atom was the O atomic position with a large distance of 3.48 Å. In ettringite, calcium cations are eight fold coordinated by four hydroxyls and four water molecules. Comparison between B-AFt and ettringite structure is given in Fig. 6. For elecroneutrality consideration, the weakly bonded O position was assumed to be hydroxyl anion for one third and water molecule for two thirds, leading to the general chemical formulae $3CaO \cdot Al_2O_3 \cdot Ca(OH)_2 \cdot 2Ca(B(OH)_4)_2 \cdot 24H_2O$ which was consistent with TGA and ICP-AES results. The channels contained two independent tetrahedral borate anion $B(OH)_4^-$, which were described by 6 non-H-atomic positions: 2 for boron (labelled B1 and B2), and 4 for oxygen of borate groups (labelled Ob11, Ob21 for apical oxygen and Ob21, Ob22 for basal oxygen atoms).

The tetrahedral coordination of boron was confirmed by Raman spectroscopy and ^{11}B NMR. The NMR spectrum (Fig. 5) exhibited a narrow and intense peak at 0.91 ppm, which showed the tetrahedral coordination of boron in the B-AFt [52]. Traces of trigonal boron were also evidenced by the broad peak at 17.9–19.5 ppm, but by integrating the peaks using the DMFit program [45], the fraction of B[III] was assessed to be less than 10%, and corresponded to a slight contamination. The B-AFt Raman spectrum in the 200–2000 cm^{-1} spectral range (Fig. 2) differed significantly from this from B-AFm. The signal observed for B-AFt was very similar to that of metaborate $NaB(OH)_4 \cdot 2H_2O$ [51], which also exhibited peaks at 421 cm^{-1} ($\delta(B-O)$), 538 cm^{-1} ($\gamma(B-O)$ and/or $[Al(OH)_6]$ [46]), 754 cm^{-1} ($\nu_3(B-O)$), 912 cm^{-1} ($\nu_3(B-O)$), 993 cm^{-1} ($\nu_{as}(B-O)$) and 1075 cm^{-1} ($\nu_{as}(B-O)$ or carbonate contamination). The absence of observable splitting for each Raman signal from borate anion showed the symmetrical similarities for the two independent $B(OH)_4$ entities.

4. Discussion

Both boron-containing B-AFm and B-AFt compounds present the crystal morphology characteristic of their respective families: platy hexagonal for B-AFm, and needle-like shape for B-AFt (Fig. 7). Their refined chemical compositions agree well with the chemical analyses (both TGA and ICP-AES): $4CaO \cdot Al_2O_3 \cdot 1/2B_2O_3 \cdot 12H_2O$ for B-AFm, and $6CaO \cdot Al_2O_3 \cdot 2B_2O_3 \cdot 33H_2O$ for B-AFt or, using the elemental oxide notation encountered in cement literature, $C_4AB_{1/2}H_{12}$ and $C_6AB_2H_{33}$. This notation hides the two different kinds of borate anions encountered. B-AFm contains planar three-fold HBO_3^{2-} anions weakly bonded at the centre of the interlayer region of the lamellar AFm structure, whereas B-AFt contains tetrahedral $B(OH)_4^-$ anions in the channel region of the columnar AFt structure. The following notations are more explicit: $[Ca_2Al(OH)_6]^+[1/2HBO_3 \cdot 3H_2O]^-$ or $3CaO \cdot Al_2O_3 \cdot CaHBO_3 \cdot 11.5H_2O$ for B-AFm, and $[Ca_3Al(OH)_6(H_2O)_9]^{3+}[2B(OH)_4 \cdot OH \cdot 2H_2O]^{3-}$ or $3CaO \cdot Al_2O_3 \cdot Ca(OH)_2 \cdot 2Ca(B(OH)_4)_2 \cdot 24H_2O$ for B-AFt. Spectroscopic investigations (Raman and ^{11}B NMR spectroscopies) have confirmed these two borate geometries. Raman spectra in the 3000 to 4000 cm^{-1} spectral range (Fig. 2), characteristic of the hydrogen bond network, show definite but broad signals due to the presence of disorder: 1/ statistic disorder between borate anion and water molecules in the interlayer region for B-AFm, and 2/statistic disorder between hydroxyl anion and water molecules in the channels for B-AFt.
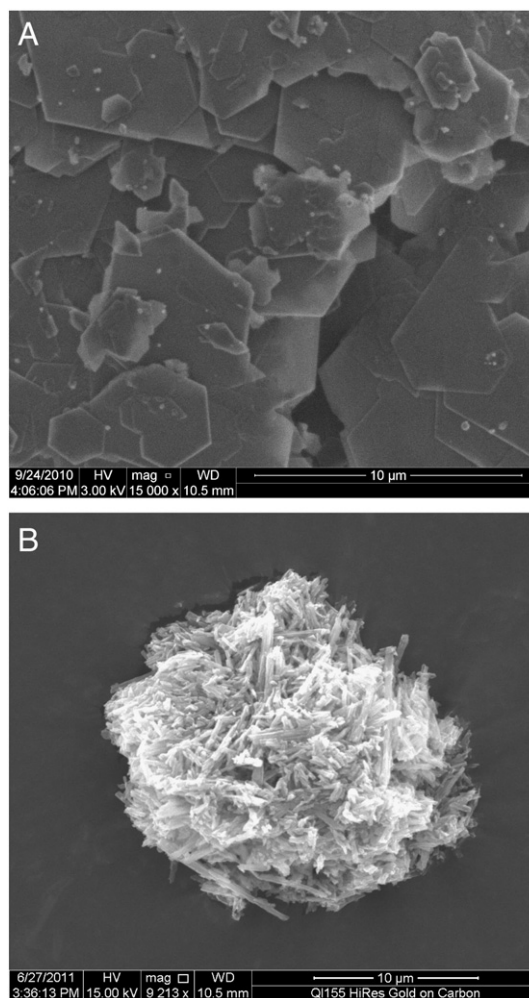

Fig. 7. SEM observation (secondary electrons) of B-AFm (A) and B-AFt crystals (B).

The B-AFm phase crystallizes in the highly symmetric rhombohedral $R\bar{3}c$ space group with an interlayer distance of 8.26 Å. This symmetry was already observed for AFm phases which insert monoatomic anions such as chloride and bromide ($Ca_2Al(OH)_6 \cdot Cl \cdot 2H_2O$ and $Ca_2Al(OH)_6 \cdot Br \cdot 2H_2O$), and also for planar trigonal carbonate anion in the case of the fully iron-substituted AFm phase ($Ca_2Fe(OH)_6 \cdot (CO_3)_{1/2} \cdot 3H_2O$). Planar HBO_3^{2-} anions are weakly bonded at the centre of the interlayer unlike carbonates and nitrates (also with a planar trigonal symmetry) which are directly bonded to Ca^{2+} cation from main layer for the pure Al-containing AFm phases [34,35]. Such a location in the interlayer region has been observed in the case of the mixed carbonate/chloride AFm phase (i.e. the carbonated Friedel's salt) [49]. On the basis of these space group considerations and anion locations, we can clearly establish the impossibility to have an ideal solid solution between the monocarboaluminate (triclinic symmetry) and B-AFm. The case of an ideal solid solution with the hemicarboaluminate (Hc) is more difficult to discuss since its crystal structure is still unknown (trigonal $R\bar{3}c$ or $R\bar{3}c$ symmetry has been assumed but carbonate anions were not located). Nevertheless, the interlayer distance of 8.2 Å for Hc [58], similar to that of B-AFm, strongly suggests the easy carbonate to borate substitution, involving hydroxyl anion, as assumed by Bothe and Brown [39,40] and corresponding to the ideal solid solution between $3CaO \cdot Al_2O_3 \cdot Ca(HO)BO_2 \cdot 11.5H_2O$ and $3CaO \cdot Al_2O_3 \cdot 1/2CaCO_3 \cdot 1/2Ca(OH)_2 \cdot 11.5H_2O$. It is interesting to note that B-AFm does not insert tetrahedral $B(OH)_4^-$ anion. Such a geometry is well known in AFm phases, but with bivalent anions: sulphate for monosulfoaluminate, and also chromate in monosulfochromate [59]. No

example of monovalent tetrahedral anion has been described yet in the AFm family. The present results from Rietveld refinement on X-ray powder data did not allow locating hydrogen atom from HBO_3 anion (and also from hydroxyl and water molecules). We were not able to discriminate if borate anions are fully ordered (with hydrogen atom located on a definite oxygen atom from HBO_3), or if the hydrogen atom can be located on the three oxygen atoms from HBO_3 (with an average partial occupancy of one third).

The borate anion in B-AFt corresponds to the monovalent tetrahedral B $(OH)_4^-$, leading to the chemical composition $3CaO \cdot Al_2O_3 \cdot Ca(OH)_2 \cdot 2Ca (B (OH)_4)_2 \cdot 24H_2O$. Compared to ettringite of composition $3CaO \cdot Al_2O_3 \cdot 3CaSO_4 \cdot 32H_2O$ which contains bivalent anions, we should find twice the number of anions in the channel region of the structure: three SO_4^{2-} anions are replaced by four B $(OH)_4^-$ anions and two OH^- anions. Whereas sulphate anions in ettringite present the up and down orientation [19], the B $(OH)_4^-$ anions are all oriented in the same direction in B-AFt: this explains the different trigonal space groups ($P31c$ for ettringite against $P3c1$ for B-AFt) and the half hexagonal c lattice parameter for the borate containing AFt (21.48 Å for ettringite against 10.70 Å for B-AFt). These different configurations are represented in Fig. 6. The anionic crystallographic positions are relatively equivalent in both structures. In the ettringite structure among the four anionic crystallographic sites, three are filled by sulphate anion and one is occupied by two water molecules. In the B-AFt case, the four anionic crystallographic sites are filled by B $(OH)_4^-$ anions, and two other hydroxyl anions (with four water molecule) are located along one channel. Whereas all channels are similar in the ettringite structure (with the sequence sulphate down–sulphate down–sulphate up–water molecules–etc…), two kinds of channels exist in B-AFt: one small channel containing borate anions only and one larger channel containing the same quantity of borate anions plus the hydroxyl/water entities (corresponding to the O site in Table 4). Calcium cations are seven fold coordinated in B-AFt (four hydroxyl + three water molecules) whereas they are eight fold coordinated in ettringite (with one supplementary water molecule). It seems that the eighth neighbouring oxygen atom has left the coordination polyhedron of Ca^{2+}, has moved to the large channel and corresponds to the hydroxyl/water crystallographic site. This explains the different water contents in ettringite and in B-AFt. Actually this difference is mainly due to water molecules bonded to the positively charged columns: $[Ca_3Al (OH)_6 \cdot 12H_2O]^{3+}$ in ettringite against $[Ca_3Al (OH)_6 \cdot 9H_2O]^{3+}$ in B-AFt.

5. Conclusion

Crystal structures of B-AFm and B-AFt phases were successfully investigated. The existence of these two ternary hydrates, synthesized under the same experimental conditions, highlights the well-known ability of boron to be 3 or 4-fold coordinated. The local structure of boron in B-AFm was shown to be planar three fold coordinated by oxygen, with one hydrogen atom located in one oxygen atom from the HBO_3^{2-} (or B $(OH)O_2$ more explicitly) borate anion. B-AFm formulae should thus be written as $3CaO \cdot Al_2O_3 \cdot CaHBO_3 \cdot 11.5H_2O$, as previously suggested by Bothe and Brown [39,40]. Contrary to other trigonal anions – carbonate and nitrate – that are directly bonded to calcium cations from the main layer in pure compounds, trigonal borate anions are weakly bonded in the centre of the interlayer region (as encountered for carbonate in mixed CO_3^{2-}/Cl^- AFm phase). It seems that this corresponds also to the case, not solved yet, of hemicarboaluminate. In B-AFt, it was shown that boron is tetrahedrally four-fold coordinated by oxygen, and that all borate groups are oriented along the same direction in the channels of the ettringite-type structure. This involves structural differences with ettringite namely in terms of symmetry (space group $P3c1$ for B-AFt and $P31c$ for ettringite) and in terms of unit cell volume (half unit cell volume for B-AFt due to a hexagonal c lattice parameter of 10.70 Å for B-AFt – compared to 21.48 Å for

ettringite – and an equivalent basal a lattice parameter). Spectroscopic analyses have confirmed these different geometries for the borate anions inserted in the AFm and the AFt phases.

References

[1] W. Lieber, Effect on inorganic admixtures on the setting and hardening of portland cement, Zement-Kalk-Gips 2 (1973) 75–79.
[2] J. Bensted, I.C. Callaghan, A. Lepre, Comparative study of the efficiency of various borate compounds as set retarders of class G oilwell cement, Cem. Concr. Res. 21 (1991) 663–668.
[3] V.S. Ramachandran, M.S. Lowery, Conduction calorimetric investigation of the effect of retarders on the hydration of portland cement, Thermochim. Acta 195 (1992) 373–387.
[4] A. Demribas, S. Karshloglu, The effect of boric acid sludges containing borogypsum on properties of cement, Cem. Concr. Res. 25 (1995) 1381–1384.
[5] L.J. Csetenyi, F.P. Glasser, Borate retardation of cement set and phase relations in the system $Na_2O–CaO–B_2O_3–H_2O$, Adv. Cem. Res. 7 (25) (1995) 13–19.
[6] C. Roux, Conditioning of Radioactive Concentrates with High Boron Content, Formulation and Characterization, Thèse de l'Université Paris Sud, France (1989).
[7] J.M. Casabonne Masonnave, Immobilization of borates and phosphates with saturated lime solutions, Solid State Ionics 56 (1993) 133–139.
[8] E. Benavides, Immobilization of evaporator concentrates with high boron content in cement matrix, SIEN'97, In: Int. Symp. on Nuclear Energy & Radioactive Waste Management, Bucarest, 2, 1997, pp. 470–471.
[9] S. Hernandez, A. Guerrero, S. Goni, Leaching of borate waste cement matrices: pore solution and solid phase characterization, Adv. Cem. Res. 12 (1) (2000) 1–8.
[10] P. Le Bescop, P. Bouniol, M. Jorda, Immobilization in cement of ion exchange resins, Mater. Res. Soc. Symp. Proc. 176 (1990) 183–189.
[11] S. Goni, A. Guerrero, Stability of calcium aluminate cement matrices mixed with borate solution, In: Proc. Int. Conf. on Calium Aluminate Cements, ISBN: 1-86125-142-4, 2001, pp. 425–435.
[12] Q. Sun, J. Wang, Cementation of radioactive borate liquid waste produced in pressurized water reactors, Nucl. Eng. Des. 240 (2010) 3660–3664.
[13] Q. Sun, J. Li, J. Wang, Effect of borate concentration on solidification of radioactive wastes by different cements, Nucl. Eng. Des. 241 (2011) 4341–4345.
[14] Q. Sun, J. Li, J. Wang, Solidification of borate radioactive resins using sulfoaluminate cement blended with zeolite, Nucl. Eng. Des. 241 (2011) 5308–5315.
[15] C. Cau Dit Coumes, S. Courtois, S. Peysson, J. Ambroise, J. Pera, Calcium sulfoaluminate cement blended with OPC: a promising binder to encapsulate low-level radioactive slurries of complex chemistry, Cem. Concr. Res. 39 (9) (2009) 740–747.
[16] J. Bensted, V. Prakash, Studies of ettringite and its derivatives, part I, Cem. Technol. 2 (1971) 73–76.
[17] W.A. Klemm, J.I. Bhatty, Fixation of heavy metals as oxyanion-substituted ettringites, In: Portland cement association research and development information, 2431a, 2002.
[18] M. Chrysochoou, D. Dermatas, Evaluation of ettringite and hydrocalumite formation for heavy metal immobilization: literature review and experimental study, J. Hazard. Mater. 136 (1) (2006) 20–33.
[19] A.E. Moore, H.F.W. Taylor, Crystal structure of ettringite, Acta Crystallogr. Struct. B 26 (1970) 386–393.
[20] H. Poellmann, H.J. Kuzel, R. Wenda, Solid-solution of ettringites. 1. Incorporation of OH^- and CO_3^{2-} in $3CaO.Al_2O_3.3CaSO_4.32H_2P$, Cem. Concr. Res. 20 (6) (1990) 941–947.
[21] P. Kumarathasan, G.J. McCarthy, D.J. Hasset, D.F. Pflughoeft-Hasset, Oxyanion substituted ettringites: synthesis and characterization; and their potential role in immobilization of As, B, Cr, Se and V, Mater. Res. Soc. Symp. Proc. 178 (1990) 83–104.
[22] G.J. McCarthy, D.J. Hasset, J.A. Bender, Synthesis, crystal chemistry and stability of ettringite, a material with potential applications in hazardous waste immobilization Mater. Res. Soc. Symp. Proc. 245 (1992) 129–140.
[23] R. Wenda, H.J. Kuzel, In: Proc. 8th International Congress on the Chemistry of Cement, Rio de Janeiro, 3, 1983, pp. 37–38.
[24] H. Poellmann, S. Auer, H.J. Kuzel, R. Wenda, Solid solution of ettringites – part II – incorporation of $B(OH)_4^-$ and CrO_4^{2-} in $3CaO.Al_2O_3.3CaSO_4.32H_2O$, Cem. Concr. Res. 23 (1993) 422–430.
[25] L.J. Csetenyi, Boron-Containing Wastes Encapsulated in Cement, PhD Thesis, University of Aberdeen, Aberdeen, UK, 1993.
[26] C.M. George, Industrial aluminous cements, In: in: P. Barnes (Ed.), Structure and Performance of Cements, Applied Science Publishers, London, 1983, pp. 415–469.
[27] S. Berger, C. Cau Dit Coumes, P. Le Bescop, D. Damidot, Influence of a thermal cycle at early age on the hydration of calcium sulphoaluminate cements with variable gypsum contents, Cem. Concr. Res. 41 (2011) 149–160.
[28] R. Allmann, Refinement of the hybrid layer structure hexahydroxoaluminodicalcium hemisulfate trihydrate $[Ca_2Al (OH)_6] [1/2SO_4.3H_2O]$, Neues Jahrb. Mineral. Monatsh. 3 (1977) 136–144.

[29] A. Terzis, S. Filippakis, K.H.J. Bruzlaff, H. Bruzlaff, The crystal structure of $Ca_2Al(OH)_6Cl.2H_2O$, Z. Krist. 181 (1987) 29.

[30] G. Renaudin, F. Kubel, J.P. Rivera, M. Francois, Structural phase transition and high temperature phase structure of Friedels salt, $3CaO.Al_2O_3.CaCl_2.10H_2O$, Cem. Concr. Res. 29 (12) (1999) 1937–1942.

[31] J.P. Rapin, G. Renaudin, E. Elkaim, M. Francois, Structural transition of Friedel's salt $3CaO.Al_2O_3.CaCl_2.10H_2O$ studied by synchrotron powder diffraction, Cem. Concr. Res. 32 (4) (2002) 513–519.

[32] M. Francois, G. Renaudin, O. Evrard, A cementitious compound with composition $3CaO.Al_2O_3.CaCO_3.11H_2O$, Acta Crystallogr C 54 (1998) 1214–1217.

[33] G. Renaudin, M. Francois, O. Evrard, Order and disorder in the lamellar hydrated tetracalcium monocarboaluminate compound, Cem. Concr. Res. 29 (1) (1999) 63–69.

[34] G. Renaudin, M. Francois, The lamellar double-hydroxide (LDH) compound with composition $3CaO.Al_2O_3.Ca(NO_3)_2.10H_2O$, Acta Crystallogr C 55 (1999) 835–838.

[35] G. Renaudin, J.P. Rapin, B. Humbert, M. Francois, Thermal behaviour of the nitrated AFm phase $Ca_4Al_2(OH)_{12}(NO_3)_2.4H_2O$ and structure determination of the intermediate hydrate $Ca_4Al_2(OH)_{12}(NO_3)_2.2H_2O$, Cem. Concr. Res. 30 (2) (2000) 307–314.

[36] J.P. Rapin, A. Walcarius, G. Lefevre, M. Francois, A double-layered hydroxide, $3CaO.Al_2O_3.CaI_2.10H_2O$, Acta Crystallogr C 55 (1999) 1957–1959.

[37] G. Renaudin, J.P. Rapin, E. Elkaim, M. Francois, Polytypes and polymorphs in the related Friedel's salt $[Ca_2Al(OH)_6]^+[X.2H_2O]^-$ halide series, Cem. Concr. Res. 34 (10) (2004) 1845–1852.

[38] R. Wenda, H.J. Kuzel, Incorporation of B-3 into calcium aluminate hydrate, Fortschr Mineral 61 (1) (1983) 217–218.

[39] J.V. Bothe, P.W. Brown, Phase formation in the system $CaO–Al_2O_3–B_2O_3–H_2O$ at 23 +/− 1 degrees C, J. Hazard. Mater. 63 (2-3) (1998) 199–210.

[40] J.V. Bothe, P.W. Brown, Phase equilibria in the system $CaO–Al_2O_3–B_2O_3–H_2O$ at 23 +/− 1 degrees C, Adv. Cem. Res. 10 (3) (1998) 121–127.

[41] http://www.accelrys.com/products/mstudio/modeling/crystallization/reflex.html.

[42] M.A. Neumann, *X-Cell*: a novel indexing algorithm for routine tasks and difficult cases, J. Appl. Crystallogr. 36 (2003) 356–365.

[43] A. Altomare, M. Camalli, C. Cuocci, I. Da Silva, C. Giacovazzo, A.G.G. Moliterni, R. Rizzi, Space group determination: improvements in EXPO2004, J. Appl. Crystallogr. 38 (5) (2005) 760–767.

[44] J. Rodriguez-Carvajal, Recent advances in magnetic structure determination by neutron powder diffraction, Physica B 192 (1–2) (1993) 55–69.

[45] D. Massiot, F. Fayon, M. Capron, I. King, S. Le Calvé, B. Alonso, J.O. Durand, B. Bujoli, Z. Gan, G. Hoatson, Modelling one and two-dimensional solid-state NMR spectra, Magn. Resson. Chem. 40 (2002) 70–76.

[46] A. Mesbah, C. Cau-dit-Coumes, F. Frizon, F. Leroux, J. Ravaux, G. Renaudin, A new investigation of the $Cl^-–CO_3^{2-}$ substitution in AFm phases, J. Am. Ceram. Soc. 94 (2011) 1901–1910.

[47] M. Hartman, S.K. Brady, R. Berliner, M.S. Conradi, The evolution of structural changes in ettringite during thermal decomposition, J. Solid State Chem. 179 (4) (2006) 1259–1272.

[48] G. Renaudin, J.-P. Rapin, E. Elkaim, M. François, Polytypes and polymorphs in the related Friedel's salt $[Ca_2Al(OH)_6]^+[X·2H_2O]^-$ halide series, Cem. Concr. Res. 34 (10) (2004) 1845–1852.

[49] A. Mesbah, J.P. Rapin, M. Francois, C. Cau-dit-Coumes, F. Frizon, F. Leroux, G. Renaudin, Crystal structures and phase transition of cementitious bi-anionic AFm-(Cl^-,CO_3^{2-}) compounds, J. Am. Ceram. Soc. 94 (1) (2011) 261–268.

[50] B.Z. Dilnesa, B. Lothenbach, G. Le Saout, G. Renaudin, A. Mesbah, Y. Filinchuk, A. Wichser, E. Wieland, Iron in carbonate containing AFm phases, Cem. Concr. Res. 41 (3) (2011) 311–323.

[51] L. Jun, X. Shuping, G. Shiyang, FT-IR and Raman spectroscopic study of hydrated borates, Spectrochim acta A 51 (4) (1995) 519–532.

[52] G.L. Turner, K.A. Smith, R.J. Kirkpatrick, E. Oldfield, Boron-11 nuclear magnetic resonance spectroscopic study of borate and borosilicate minerals and of a boro-silicate glass, J. Magn. Reson. 67 (1986) 544–550.

[53] P.J. Bray, J.O. Edwards, J.G. O'Keefe, V.F. Ross, I. Tatsuzaki, Nuclear magnetic reso-nance studies of B11 in crystalline borates, J. Chem. Phys. 35 (1961) 435–442.

[54] S. Kroeker, J.F. Stebbins, Three-coordinated boron-11 chemical shifts in borates, Inorg. Chem. 40 (2001) 6239–6246.

[55] C. Gervais, F. Babonneau, High resolution solid state NMR investigation of various boron nitride preceramic precursors, J. Organometallic Chem. 657 (2002) 75–82.

[56] K.P. Peil, L.G. Galya, G. Marcellin, Acid and catalytic properties of non stoichiometric aluminium borates, J. Catal. 115 (1989) 441–451.

[57] G. Renaudin, Y. Filinchuk, J. Neubauer, F. Goetz-Neunhoeffer, A comparative structural study of wet and dried ettringite, Cem. Concr. Res. 40 (2010) 370–375.

[58] R. Fischer, H.J. Kuzel, Cem. Concr. Res. 12 (1982) 517.

[59] S.M. Leisinger, B. Lothenbach, G. Le Saout, C.A. Johnson, Thermodynamic model-ing of solid solutions between monosulfate and monochromate $3CaO·Al_2O_3·Ca[(CrO_4)_x(SO_4)_{1-x}]·nH_2O$, Cem. Concr. Res. 42 (2012) 158–165.